Industrial Chemistry & Materials

ROYAL SOCIETY OF CHEMISTRY

PAPER

View Article Online
View Journal

Cite this: DOI: 10.1039/d6im00093b

Zeolite-confined ionic liquid enables on-demand active bromine generation for thermally robust and reduced-dosage antimicrobial materials

Jingkun Zhang,[ab] Hao Ling,[c] Haidi Liu,[ab] Yiyang Gong,[ad] Guangxin Ma,[ab] Ning Han,[ab] Hongyan He *[ab] and Yunfa Chen *[ab]

The proliferation of multidrug-resistant pathogens and persistent microbial contamination in industrial settings necessitates the development of robust, processable, and highly efficient antimicrobial additives. Herein, we report a HZSM-5 zeolite/ionic liquid composite, constructed by confining and chemically anchoring a bromine-containing ionic liquid (IL) within the microporous channels of HZSM-5 zeolite. This unique structure imparts exceptional thermal stability, with the confined IL withstanding temperatures exceeding 330 °C and retaining full bactericidal activity after high-temperature (250 °C) processing, demonstrating its suitability for industrial melt-processing applications. Then, a potent synergistic mechanism wherein the host–guest system catalytically activates molecular oxygen to generate reactive oxygen species (ROS), which in turn oxidizes the bromide anions (Br^-) into elemental bromine (Br_2) *in situ*, is proposed. This self-enhancing cycle, confirmed by XPS, EPR, and UV-vis spectroscopy, enables the composite to achieve superior bactericidal efficacy against a range of pathogens, including *MRSA*, at a significantly reduced IL dosage compared to the pure IL and conventional agents. The mechanism involves a multi-pronged attack combining electrostatic adsorption, dual-action membrane disruption (IL and Br_2), and an intracellular ROS burst. This work presents a new design paradigm for creating thermally stable, high-performance antimicrobial materials with significant potential to address pressing industrial challenges in polymer processing, medical devices, and functional coatings.

Received 13th March 2026,
Accepted 13th April 2026

DOI: 10.1039/d6im00093b

rsc.li/icm

Keywords: Ionic liquids; Confinement; Antibacterial activity; Bromide oxidation; Synergistical effect.

1 Introduction

The escalating threat of antibacterial contamination and the rise of multidrug-resistant (MDR) pathogens pose a significant challenge across numerous industrial sectors, from polymer manufacturing and medical device fabrication to food packaging and protective coatings.[1,2] The incorporation of antimicrobial agents into materials is an effective strategy to mitigate these risks.[3] However, the existing arsenal of antimicrobial agents faces a critical trade-off between efficacy, processability, and long-term viability, creating a pressing industrial demand for a new generation of materials that can overcome these limitations.

Conventional organic antimicrobial agents, such as quaternary ammonium compounds (QACs), undergo thermal degradation *via* Hofmann elimination at temperatures well below typical processing thresholds, often starting around 180 °C.[4] Similarly, popular inorganic agents like silver nanoparticles (AgNPs) suffer a dramatic loss of efficacy when subjected to high temperatures, as high temperature can result in particle agglomeration, which reduces the available active surface area and diminishes their antibacterial activity.[5] Consequently, there is a significant industrial need for a new class of robust, "processable" antimicrobial agents that can be integrated into a material matrix prior to thermal processing and remain highly active in the final product.

Ionic liquids are a class of molten salts, typically composed of organic cations and various anions, with melting points below 100 °C.[6] As a broad class of materials, their unique molecular structures endow them with many valuable properties including negligible volatility, good ionic conductivity, high thermal stability, *etc.*, compared to traditional molecular solvents.[7,8] Recently, certain ILs, especially imidazolium-based derivatives with an alkyl chain constituted by 12 to 16 carbon atoms,[9–12] have

[a] State Key Laboratory of Mesoscience and Process Engineering, Institute of Process Engineering, Chinese Academy of Sciences, Beijing 100190, China. E-mail: hyhe@ipe.ac.cn, chenyf@ipe.ac.cn
[b] Center of Materials Science and Optoelectronics Engineering, University of the Chinese Academy of Sciences, Beijing 100049, China
[c] Beijing National Laboratory for Condensed Matter Physics, Institute of Physics, Chinese Academy of Sciences, Beijing 100190, China
[d] School of Materials Science and Engineering, Shenyang University of Chemical Technology, Shenyang, Liaoning, 110142, China

been found to have outstanding antimicrobial activity. Differing from the traditional antibacterial materials that target specific metabolic pathways, the primary antibacterial mechanism of ILs involves a physical disruption of the cell membranes.[10,13] The lipophilic alkyl chains insert into and destabilize the lipid bilayer, leading to an increasing permeability and eventual cell lysis.[9,14] This non-specific, membrane-centric action makes it considerably more difficult for bacteria to evolve defense mechanisms against ILs.[15–17]

Despite these potentials, the practical application of ILs is impeded by two primary limitations. The first concerns their thermal degradation temperature. Many long-chain ILs are insufficient for high-temperature processes, such as melt-processing of antibacterial polymers.[18–21] The second one relates to the antibacterial activity of most ILs being predominantly derived from the cations, which can disturb the lipid bilayer of the bacterial cell membrane, thereby increasing the permeability of cell membranes and leading to cell lysis,[22–24] while the anions (*e.g.* bromide, chloride, and iodide) are often used to regulate physical properties and remain biologically inert, contributing little to the overall antibacterial action.[9,10,25]

Various strategies including anion regulation, construction of IL-based nanohybrids and combining ILs with other materials for synergistic effects have been explored to address these shortcomings.[18,26] For instance, substituting halogen ions with large-sized anions of tetrafluoroborate (BF_4^-) and 1,3-dimethyl-5-sulfoisophthalate (DMSIP) can improve the thermal stability of ILs with alkyl chain length from C_9 to C_{20}, enabling their application in PVC processing technology, although this modification can result in a certain loss of antibacterial performance.[27] Functionalizing the surface of nanomaterials such as Ag, Cu, Au, ZnO, multiwalled carbon nanotubes, graphene oxide, g-C_3N_4, *etc.* with imidazolium-based ILs containing alkyl chain length from C_2 to C_{16} can produce hybrids with remarkably enhanced thermal stability and synergistic antibacterial performance.[28–37] Other noteworthy approaches involve the use of porous materials like organoclays, mesoporous silica, and cyclodextrin as nanocarriers to host long alkyl chain ILs, which can improve their thermal stability as well as create controlled-release systems.[30,38–44]

HZSM-5, a synthetic zeolite with unique porosity and acidic properties, is widely used in petrochemical processes such as catalytic cracking, isomerization, and aromatization. Recently, one of the emerging applications of HZSM-5 involves the activation of methane using halogens (X_2, X = Cl, Br) for the production of high-value chemicals and liquid fuels, where the Br_2 used can be *in situ* generated by the oxidation of HBr over HZSM-5.[45] Furthermore, HZSM-5 with MFI topological structure possesses excellent thermal stability.[46] Under the high-temperature, highly corrosive, and high-humidity conditions of HBr oxidation, its framework is resistant to collapse and dealumination, enabling long-term maintenance of catalytic activity and structural integrity.[47,48] In addition, its microporous structure can enrich HBr and O_2, stabilize reaction intermediates, and thus enhance the selectivity of Br_2 formation.[45]

Herein, we propose a novel approach to overcome the limitations of ILs by preparing a composite material through the impregnation of 1-tetradecyl-3-methylimidazolium bromide ionic liquid (a long-chain IL with established antimicrobial activity) into the pore channels of HZSM-5 zeolite. The confinement of the IL within the zeolite's acidic sites may not only enhance the material's thermal stability but also induce a synergistic antibacterial mechanism. In this context, protons transfer from the Brønsted acid sites of HZSM-5 to the ionic liquid, rendering the imidazolium cations of the ionic liquid more electron-rich, thereby enabling the activation of adsorbed oxygen, leading to the *in situ* oxidation of bromide ions to elemental bromine. This process could create a potent synergistic effect, where the newly formed elemental bromine damages the outer membrane of Gram-negative bacteria, facilitating the penetration of the imidazolium cations to disrupt the inner membrane. This study details the synthesis and characterization of the HZSM-5–IL composites, evaluates their enhanced thermal stability and antibacterial efficacy against both Gram-positive and Gram-negative pathogens, and elucidates the new synergistic mechanism responsible for their superior performance.

2 Results and discussion

2.1 Synthesis and characterization of HZSM-5–*n*IL composites

A series of HZSM-5–*n*IL composites, with *n* representing the mass ratio of IL to the HZSM-5 zeolite (*n* = 0.25, 0.35, 0.5, 1 and 2), were prepared *via* an impregnation method. The color of the composites visually changed from white to brown, which may be attributed to the change in their components (Fig. S1).

The textural properties of the composites and pure HZSM-5 were investigated using the N_2 adsorption–desorption isotherms at 77 K. As depicted in Fig. 1a, HZSM-5 exhibited a typical type I isotherm, characteristic of a microporous structure.[49] Upon IL incorporation, a significant suppression of the initial N_2 uptake at low relative pressures ($P/P_0 < 0.1$) was observed across all composites, coupled with a drastic reduction in the micropore volume (Fig. 1a and Table S1). This indicates that IL molecules have successfully entered into and physically occupied the microporous channels, blocking access to N_2 molecules. Fourier-transform infrared (FT-IR) spectroscopy (Fig. 1b) indicates that as the IL loading decreased, the characteristic peaks attributed to the imidazolium head groups diminished gradually, whereas the peaks from the alkyl tails showed only a minor reduction. This suggests a preferential orientation where the imidazolium head groups are selectively embedded deep within the zeolite's microporous channels, and this result is further substantiated by the SEM/EDS mapping (Fig. S2) as a diffuse nitrogen signal originating from imidazolium head groups was observed. X-ray diffraction (XRD) analysis not only confirmed the preservation of the MFI framework structure post-incorporation but also revealed a saturation point for this confinement (Fig. S3). For composites with an IL content $n \geq 0.5$, the emergence of a new diffraction peak at ~7°,

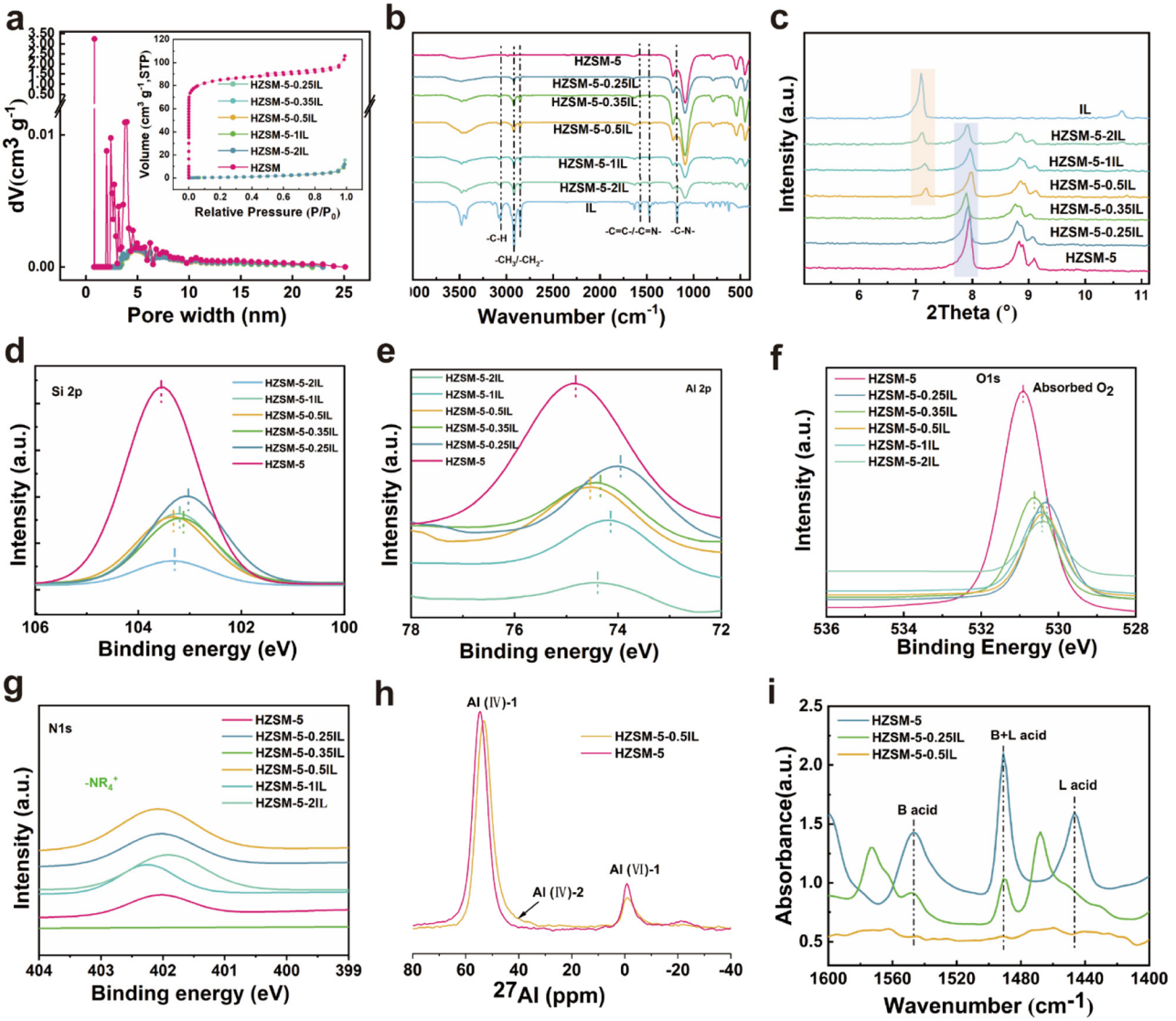

Fig. 1 Characterization of the structure and the confined environment of HZSM-5–*n*IL. (a) Pore size distributions from BJH adsorption. The inset shows the N_2 adsorption–desorption isotherms and pore size distributions from BJH adsorption; (b) FT-IR spectra; (c) partial enlarged XRD pattern and (d) XPS spectra of Si 2p; (e) XPS spectra of Al 2p; (f) XPS spectra of O 1s; (g) XPS spectra of N 1s; (h) ^{27}Al NMR of HZSM-5 and HZSM-5–0.5IL. (i) Py-FTIR of HZSM-5, HZSM-5–0.5IL and HZSM-5–0.25IL.

corresponding to the semi-crystalline structure of the pure IL, signifies that the micropores have become saturated (Fig. 1c). This result distinguishes two distinct populations of IL: a confined population within the pores and an excess population accumulating on the external surface.

After establishing physical confinement, the chemical nature of the host–guest interaction is elucidated. A slight but consistent shift of the HZSM-5 (101) peak to a lower angle in the XRD patterns (Fig. 1c) pointed to a lattice expansion, indicating a strong interaction that perturbs the host framework. This interaction was then revealed by X-ray photoelectron spectroscopy (XPS). A significant negative shift in the Si 2p and Al 2p binding energies of the framework (Fig. 1d and e) and a decrease in the O 1s (Fig. 1f) shoulder peak characteristic of acidic hydroxyl protons were observed. Concurrently, a positive shift in the N 1s signal (Fig. 1g) demonstrated the protonation of the imidazolium ring. These concerted electronic shifts indicate a proton transfer from the Brønsted acid sites of the zeolite to the confined IL. Solid-state ^{27}Al MAS NMR spectroscopy (Fig. 1h) was used to further corroborate the result. The up-field shift of the tetrahedrally coordinated aluminium signal proved an increase in the electron shielding of the framework Al nuclei following deprotonation of imidazolium head groups and the emergence of a new shoulder peak adjacent to the main Al(Ⅳ) signal suggests a structural distortion of the aluminium sites,[50] likely caused by strong electronic effects from the now tightly-bound imidazolium cations. Pyridine-adsorbed FT-IR (Py-FTIR) spectroscopy (Fig. 1i) showed that the near-complete disappearance of the characteristic Brønsted acid site bands confirms the firm occupation of the imidazolium cations. These results demonstrate that the IL is not merely

physically entrapped but is chemically anchored within the HZSM-5 pore channels *via* a strong host–guest interaction involving proton transfer.

2.2 High-temperature processability and enhanced antibacterial efficacy

A critical industrial requirement for antibacterial materials is the ability to withstand high-temperature processing. The established host–guest interaction imparts remarkable thermal stability to the composite materials. Thermogravimetric analysis (TGA) indicates that, in contrast to the pure IL, which decomposed in a single, continuous loss step, the HZSM-5–*n*IL composites exhibited a distinct two-stage weight loss profile (Fig. 2a). The first stage is attributed to the decomposition of the unconfined IL molecules residing on the external surface of the HZSM-5 zeolite, occurring at temperatures comparable to the decomposition of the pure IL. The second stage, however,

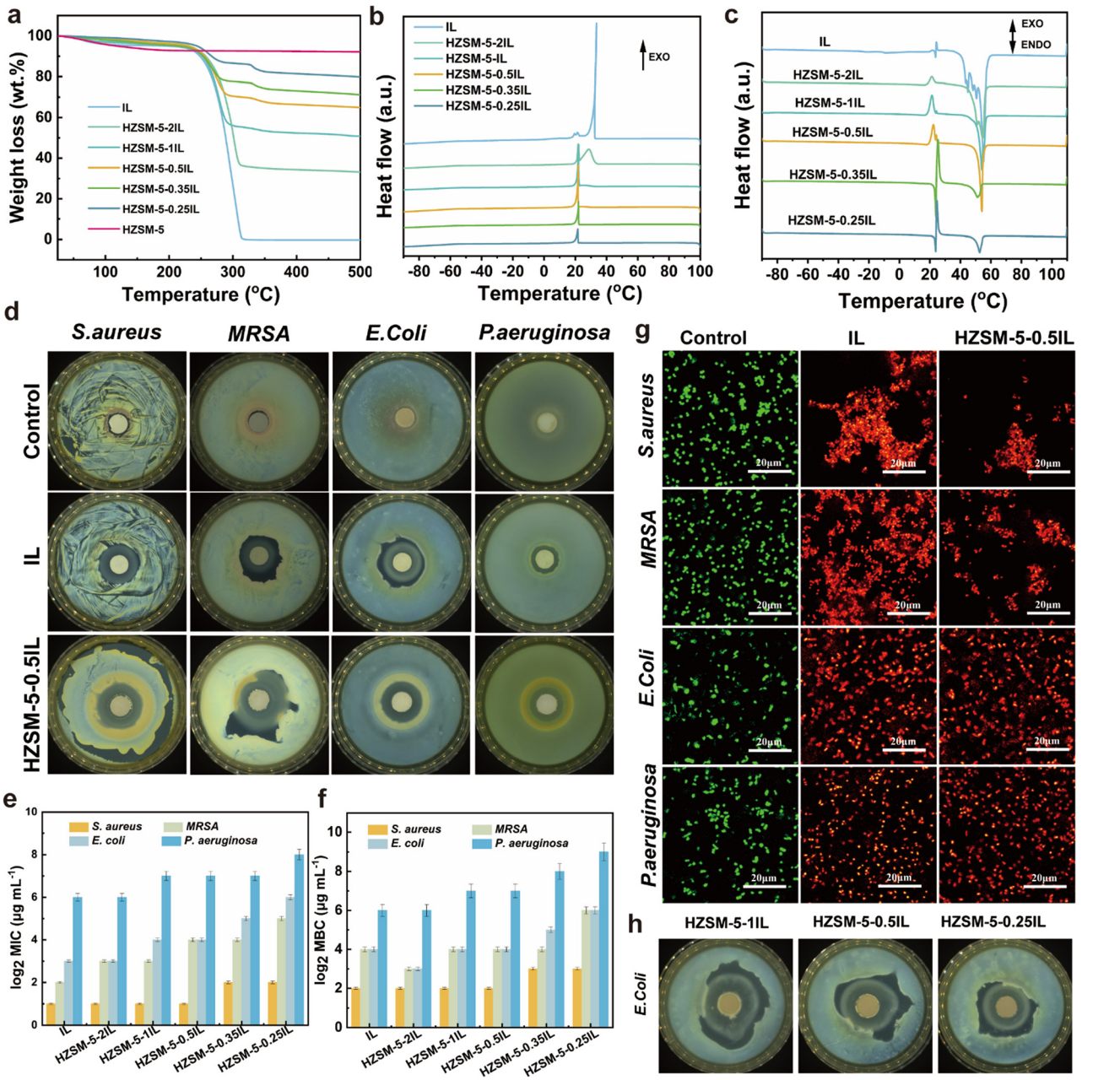

Fig. 2 (a) TGA curves; (b) DSC cooling curves; (c) DSC heating curves; (d) the inhibition zone of *S. aureus*, *MRSA*, *E. coli* and *P. aeruginosa* treated with IL (0.05 g) and HZSM-5–0.5IL (0.1 g); (e) $\log_2$ MIC values of *S. aureus*, *MRSA*, *E. coli* and *P. aeruginosa* treated with IL and HZSM-5–0.5IL (18 h); (f) $\log_2$ MBC values of *S. aureus*, *MRSA*, *E. coli* and *P. aeruginosa* treated with IL and HZSM-5–0.5IL (18 h); (g) fluorescence microscopy images of *E. coli* and *S. aureus*, *MRSA* and *P. aeruginosa* cells subjected to IL and HZSM-5–0.5IL (25 μg mL^{-1}) at 37 °C for 30 min; (h) the inhibition zone of *E. coli* treated with 0.1 g HZSM-5–1IL, HZSM-5–0.5IL HZSM-5–0.25IL after 300 °C heating. Error bars were obtained with three parallel samples.

corresponds to the degradation of the IL confined within the zeolite's micropores. The onset decomposition temperatures (T_{onset}) of this second stage for the HZSM-5–*n*IL composites are 352.5, 351.4, 314.3, 334.2, and 328.4 °C for n = 2, 1, 0.5, 0.35, and 0.25, respectively. Notably, all composites exhibit substantially higher T_{onset} values than the pure IL (T_{onset} = 281.3 °C), demonstrating that zeolite confinement significantly enhances the thermal stability of the IL. The variation in T_{onset} with IL loading ratio is attributed to the changing distribution of confined *versus* surface-adsorbed IL species: at intermediate loadings, a larger fraction of IL resides on the external surface of the zeolite and is thus less protected by the pore framework, resulting in a comparatively lower T_{onset}.

To further elucidate the physical state of IL within the HZSM-5 pore channel, comparative differential scanning calorimetry (DSC) measurements were performed on the pure IL and the HZSM-5–*n*IL composites. As shown in Fig. 2b, the cooling curve of the pure IL exhibits a sharp crystallization exothermic peak at ~33 °C, whereas no crystallization peak is observed for the fully confined HZSM-5–0.25IL, indicating suppression of crystallization due to the nanoconfinement effect.[7,51] This is further supported by the second heating scans (Fig. 2c): while the pure IL shows a cold crystallization exothermic peak at ~24 °C and multiple melting and phase transition endothermic peaks at 40–60 °C (main peak at ~55 °C), the confined composite exhibits neither cold crystallization nor characteristic melting peaks. Instead, only a slightly depressed endothermic transition at ~52 °C is observed, which is consistent with the Gibbs–Thomson melting point depression of nanoconfined systems.[7] These thermodynamic results confirm that IL is confined within the micropores of HZSM-5 in an amorphous state, providing the structural basis for its sustained release and long-lasting antibacterial activity.

Subsequently, a series of assays including disk diffusion assay, minimal inhibitory concentration (MIC) and minimal bactericidal concentration (MBC) were conducted against four representative bacterial strains including *E. coli* (Gram-negative), *S. aureus* (Gram-positive), *MRSA* (multidrug resistant bacteria) and *P. aeruginosa* (biofilm forming). The composites demonstrated significantly enhanced antibacterial efficacy compared to the pure IL (Tables S2 and S3). The HZSM-5–1IL composite, which has an IL loading equivalent to the pure IL dosage tested, produced a significantly larger inhibition zone against the resilient *P. aeruginosa* (22.55 mm) compared to the pure IL (18.05 mm) (Fig. 2d and Table S2). In addition, the HZSM-5–0.5IL composite, which contains only one-third the amount of IL used in the pure IL test, exhibited MBC values against *E. coli*, *S. aureus*, and the multidrug-resistant *MRSA* that were almost comparable to those of the pure IL (Fig. 2e and f and Table S3). Even for the highly robust, biofilm-forming *P. aeruginosa*, the MBC value for HZSM-5–0.5IL was only twice that of the pure IL. This enhanced performance was further visually confirmed by confocal laser scanning microscopy (CLSM), which showed that after just 30 minutes of exposure, a visibly higher proportion of bacteria treated with HZSM-5–0.5IL exhibited red fluorescence (indicating membrane damage and cell death) compared to those treated with the pure IL (Fig. 2g), indicating a faster and more potent bactericidal action. Finally, to simulate realistic high-temperature processing conditions, the HZSM-5–0.5IL composite was placed in a muffle furnace and heated at a ramp rate of 10 °C min^{-1} to 250 °C, held at this temperature, and subsequently allowed to cool to room temperature. The antibacterial activity of the recovered composite was evaluated against *E. coli* using the disk diffusion assay. As depicted in Fig. 2h, the heat-treated composite retained its antibacterial activity, indicating its high temperature stability.

2.3 *In situ* generation of elemental bromine (Br_2)

The enhanced antibacterial performance at a reduced IL dosage strongly implies the existence of a secondary, highly potent antimicrobial agent generated *in situ*. This agent is supposed to be elemental bromine (Br_2), whose formation is a catalytic consequence of the unique confined environment.

To directly probe the generated bromine species, the HZSM-5–*n*IL composite was immersed in ethanol for two days, and the resulting brown supernatant was analyzed by UV-vis spectroscopy. The spectrum revealed a complex mixture of bromine species (Fig. 3a). Broad absorption bands centered at approximately 470 nm and 392 nm were observed, which were characteristic of molecular bromine (Br_2) in polar protic solvents and aqueous solution. Additionally, distinct peaks were identified at ~267 nm and shoulder peaks at ~330 nm, corresponding to the tribromide ion (Br_3^-) and hypobromous acid (HOBr), respectively. The absence of absorption bands at higher energy levels indicates that no higher-valent bromine oxides were formed. This direct spectroscopic result confirms the generation of reactive bromine species, predominantly Br_2, and is in excellent agreement with the XPS results, which detected only Br^0 and Br^- states (Fig. 3b).

Quantitative evidence was subsequently provided by high-resolution XPS of the Br 3d region (Fig. 3c). Deconvolution of the Br 3d spectrum for the composite materials revealed the emergence of a new doublet at a higher binding energy, corresponding to neutral Br^0 atoms in Br_2, which was clearly distinguishable from the original Br^- signal of the ionic liquid (Fig. 3d and e). Critically, the relative content of this elemental bromine was found to be highest in the HZSM-5–0.5IL sample (Fig. 3e), establishing a direct correlation between a specific composition and the maximal generation of the secondary antimicrobial agent. This compositional dependence suggests that the oxidation of Br^- is not a spontaneous process but is instead catalyzed by the host–guest interaction.

The mechanistic origin of this catalytic activity was traced to the generation of reactive oxygen species (ROS). As established before, the strong host–guest interaction and proton transfer create unique, electron-rich catalytic centres within the zeolite framework. These centres are capable of

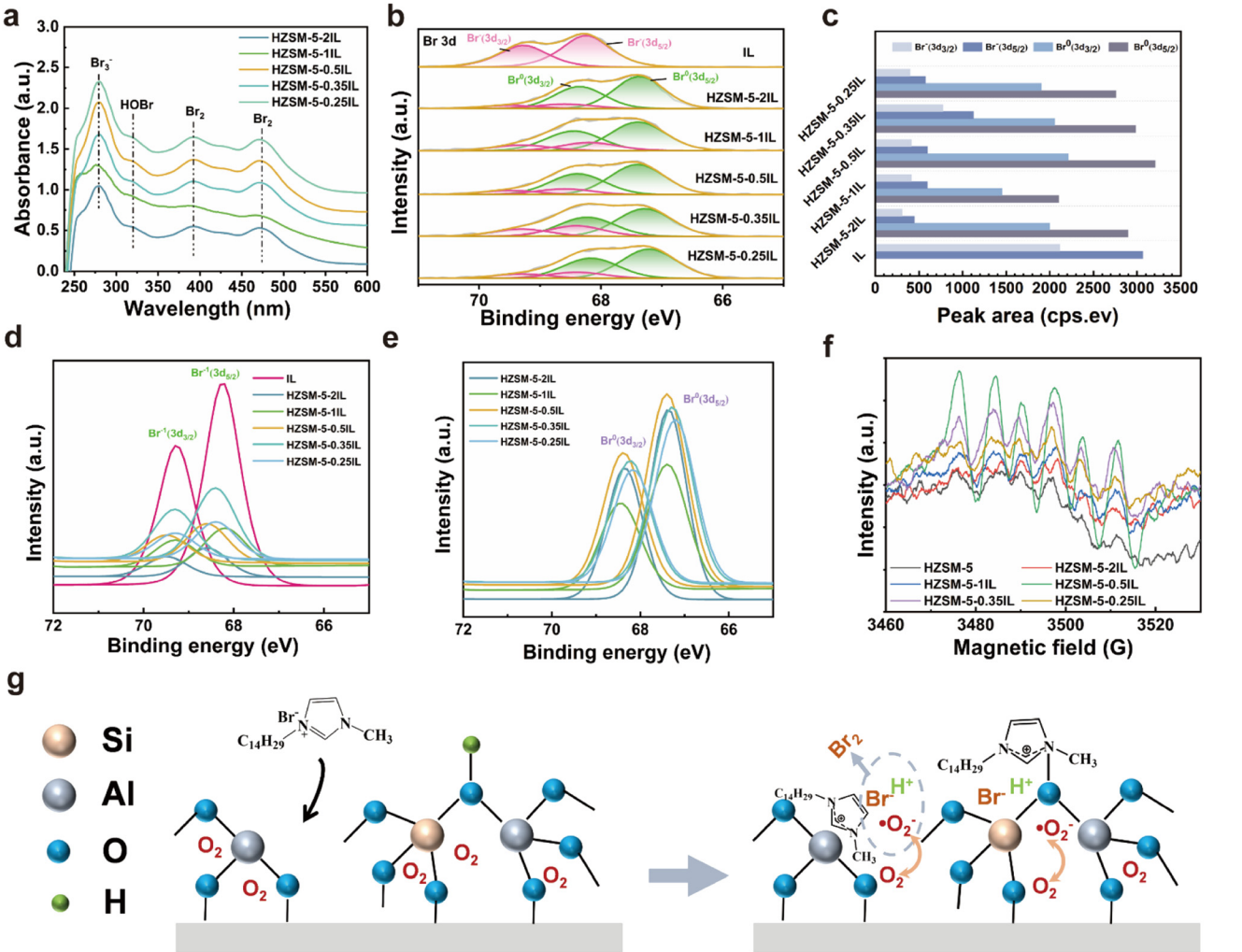

Fig. 3 Generation of Br_2. (a) UV-vis of bromine species for HZSM-5–*n*IL; (b) XPS spectra of Br 3d; (c) integrated areas of Br 3d deconvoluted peaks at different oxidation states (Br^- and Br^0); (d) XPS spectra of Br^- 3d orbitals for IL and HZSM-5–*n*IL composites; (e) XPS spectra of Br^0 3d orbitals for IL and HZSM-5–*n*IL composites; (f) EPR spectra of DMPO–O_2^- for HZSM-5–*n*IL composites; (g) the schematic mechanism of the generation of Br_2 for HZSM-5–*n*IL composites, color code: golden = silicon, grey = aluminum, blue = oxygen, green = hydrogen.

activating adsorbed molecular oxygen (O_2) (Fig. S8), a process confirmed by Electron Paramagnetic Resonance (EPR) spectroscopy, which detected a characteristic signal for the superoxide anion radical ($\cdot O_2^-$) (Fig. 3f). Moreover, the intensity of this $\cdot O_2^-$ signal is similar to the trend observed in the XPS data, peaking in the HZSM-5–0.5IL sample. This direct correlation provides compelling evidence that $\cdot O_2^-$ is the key intermediate species responsible for the subsequent oxidation of bromide.

Based on these results, a three-step reaction mechanism is proposed for the *in situ* generation of Br_2 (Fig. 3g). First, the catalytically active sites within the confined environment activate molecular oxygen to the superoxide radical ($\cdot O_2^-$) (eqn (1)). Second, within the strongly acidic nanochannels of HZSM-5, the initially formed $\cdot O_2^-$ is readily protonated to the more potent and reactive hydroperoxyl radical ($HO_2\cdot$) (eqn (2)). Finally, this powerful oxidizing radical efficiently oxidizes two bromide ions (Br^-) to elemental bromine (Br_2) (eqn (3)).

$$O_2 + e^- \rightarrow \cdot O_2^- \quad (1)$$

$$\cdot O_2^- + H^+ \rightarrow HO_2\cdot \quad (2)$$

$$HO_2\cdot + 6H^+ + 6Br^- \rightarrow 3Br_2 + 4H_2O \quad (3)$$

This newly formed Br_2 is stabilized within the hydrophobic nanopores of the zeolite, preventing its immediate volatilization and enabling a controlled, sustained release. It is important to address the potential safety concerns regarding the *in situ* generated Br_2. While bulk elemental bromine is known to be toxic and corrosive, the safety of our composite is ensured by the nanoconfinement effect of the zeolite matrix. The strong host–guest interactions and the steric hindrance of the long alkyl chains within the pore channels significantly restrict the free diffusion of Br_2, permitting only a slow and sustained release. Consequently, the steady-state concentration of free Br_2 released into the surrounding environment is maintained at a

trace, sub-toxic level. Based on our quantitative calculations, even assuming 100% conversion of bromide ions, the maximum theoretical Br_2 concentration at the bactericidal dosage (*e.g.*, an MBC of 32 μg mL^{-1} for *E. coli*) is only 1.17 μg mL^{-1}. According to the World Health Organization (WHO) and relevant environmental safety guidelines, an LC_{50} of 240 ppm (1569 mg m^{-3}) has been reported in mice (strain and sex not specified) exposed to bromine vapour for 2 hours (PHE, 2009).[52] This trace level is highly effective for eradicating bacteria, yet falls well below the cytotoxicity threshold that could trigger acute toxicity or allergic reactions in mammalian cells. This controlled-release mechanism ensures that the material achieves superior antibacterial efficacy while maintaining a high safety profile.

2.4 Synergistic antibacterial mechanism

Having established the presence of the IL, *in situ* generated Br_2 and $\cdot O_2^-$, the multi-target synergistic mechanism that enables the composite to achieve superior bactericidal efficacy at a reduced dosage can be demonstrated.

The initial interaction is governed by electrostatic attraction. Both the pure IL and the HZSM-5–0.5IL composite successfully adsorbed onto the negatively charged bacterial surfaces, as evidenced by the reversal of the surface zeta potential to positive values (Fig. 4a). This step concentrates the antimicrobial agents directly at the site of action.

Then, following adsorption onto the bacterial cell surface, synergistic membrane disruption commences through the concerted action of three antibacterial components. First, the IL component acts as a classic amphiphilic surfactant. Its hydrophobic alkyl tails insert into the lipid bilayer, disrupting membrane fluidity and integrity, leading to physical leakage. Concurrently, the *in situ* generated Br_2 and $\cdot O_2^-$ launch a secondary, more aggressive chemical attack. As potent oxidizing agents, Br_2 and $\cdot O_2^-$ directly oxidize membrane lipids and proteins, leading to chemical perforation. SEM images visualized this severe morphological damage (red arrows in Fig. 4b). Notably, for *MRSA*, the membrane vesicles (MVs) of composite-treated bacteria possess extensive porosity, a stark contrast to the denser MVs on IL-treated cells.[53,54] In the case of *P. aeruginosa*, the composite also demonstrated enhanced efficacy, stimulating a more outer membrane vesicle (OMV) formation compared to the pure IL.[53,54] This intensified vesiculation, a known bacterial stress response, can lead to a 'leaky' phenotype and ultimately trigger apoptosis in the parent cells.[55] The synergistic effect of the IL, Br_2 and $\cdot O_2^-$ appears to amplify this stress signal, and induce apoptosis of the parent cells. This remarkable distinction is attributed to the additional, potent dissolution effect of Br_2, a mechanism distinct from the IL's primary action as a surfactant.[9,56,57] This combined physical and chemical damage to the cell membrane is far more destructive than the action of the IL alone.

Intracellular ROS burst: it has been confirmed in the literature that after membrane disruption, DNA binding may induce bacteria to have a stress response and release a large amount of ROS,[58] which in turn may damage the cell membrane directly or result in bacterial apoptosis. The synergistic membrane damage overwhelms the cell's antioxidant defense systems, triggering a massive intracellular oxidative burst. Using a DCFH-DA probe, a substantial increase in intracellular ROS levels was observed for all four tested bacterial strains after a 30 minute incubation (Fig. 4c). Obviously, the ROS generation was significantly more pronounced in cells treated with HZSM-5–0.5IL compared to the pure IL. This indicates that the combination of membrane disruption by the IL and the oxidative damage from Br_2 and $\cdot O_2^-$ triggers a more intense intracellular oxidative stress.

Cell death: the oxidative damage to DNA, proteins, and other vital intracellular components, initiated by the overwhelming ROS burst, ultimately leads to rapid and irreversible cell death.

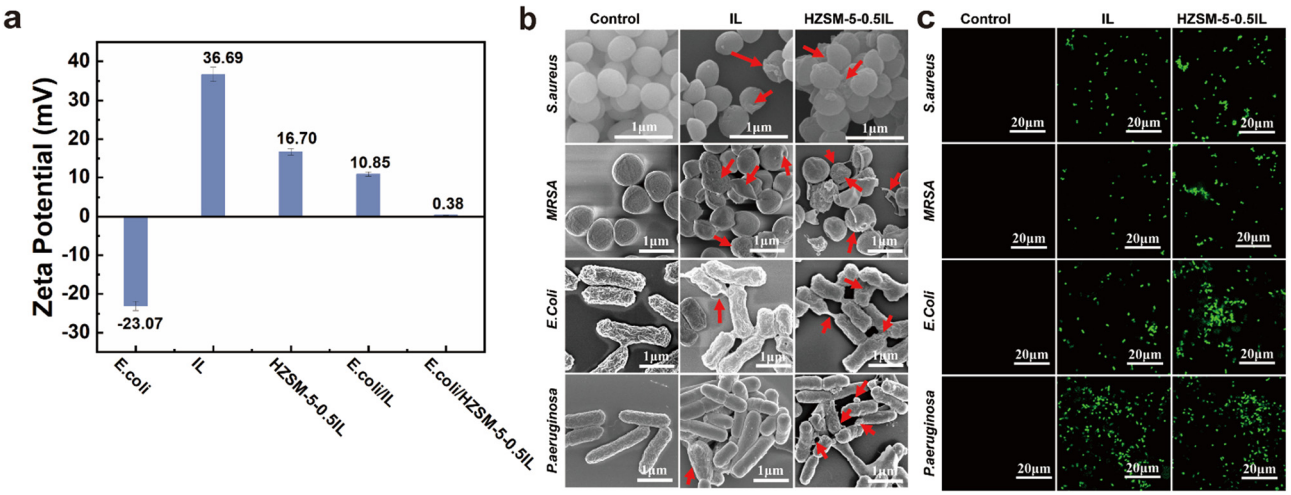

Fig. 4 Antibacterial mechanism of HZSM-5–*n*IL. (a) Zeta potential of IL and HZSM-5–0.5IL; (b) SEM images of *S. aureus*, *MRSA*, *E. coli* and *P. aeruginosa* subjected to IL and HZSM-5–0.5IL (50 μg mL^{-1}) at 37 °C for 1 h; (c) fluorescence microscopy images of *S. aureus*, *MRSA*, *E. coli* and *P. aeruginosa* using DCFH-DA as a ROS probe for IL and HZSM-5–0.5IL. Error bars were obtained with three parallel samples.

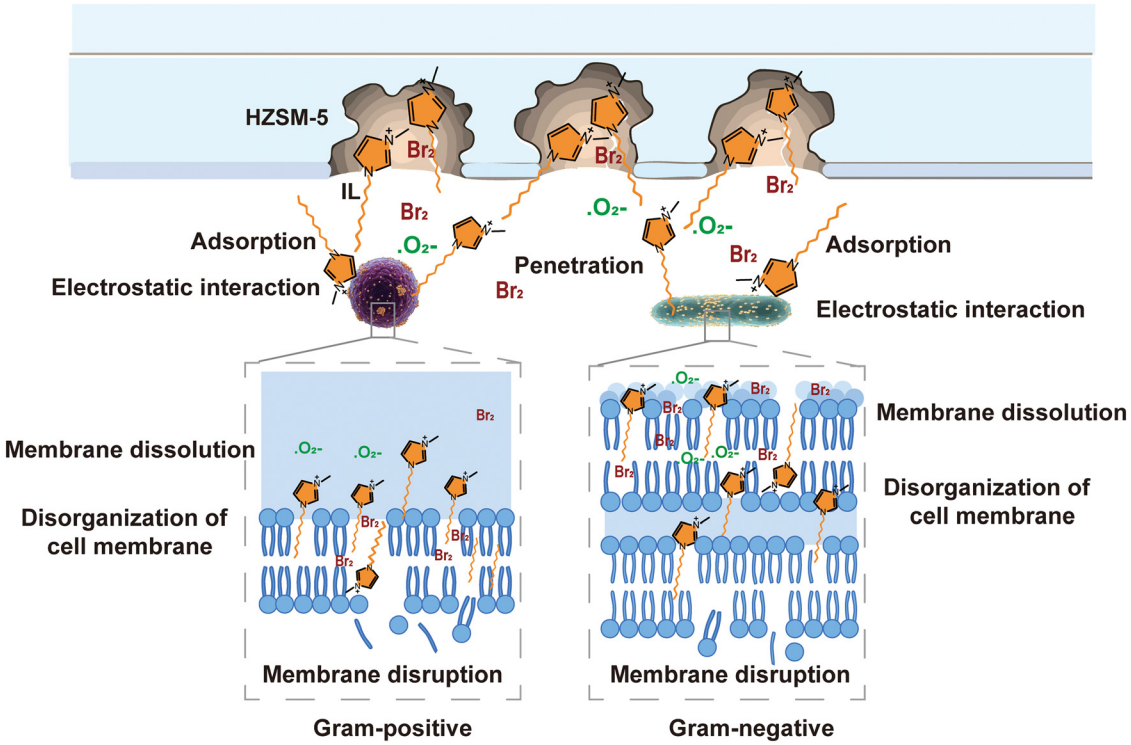

Fig. 5 The schematic of the synergistic antibacterial mechanism for HZSM-5–*n*IL composites.

To sum up, the antibacterial mechanism of the HZSM-5–0.5IL composite is a multiple-attack synergy including electrostatic adsorption, dual-action membrane disruption (physical *via* IL, chemical *via* Br_2 and $\cdot O_2^-$), and a subsequent overwhelming intracellular ROS burst (Fig. 5). This synergistic mechanism, rooted in the material's unique host–guest architecture, fully explains the superior antibacterial performance of the composite material at a reduced active agent dosage.

3 Conclusions

In summary, to more efficiently utilize the antibacterial properties of ionic liquids, we employed a green and innovative strategy to design self-catalytic HZSM-5–IL composites to achieve the *in situ* generation of Br_2 from ionic liquid anions, implementing synergistic antibacterial effects. The resulting HZSM-5–0.5IL composite material not only retains the membrane-disrupting properties of the ionic liquid but also integrates the potent oxidative damage of *in situ* generated Br_2. This synergistic mechanism leads to significantly enhanced efficacy against a broad spectrum of pathogens, including the tough *MRSA* and the biofilm-forming *P. aeruginosa*. The optimized composite (HZSM-5–0.5IL) loaded only one-third of the pure IL, its MBC values against *E. coli*, *S. aureus* and *MRSA* were comparable to those of the pure IL, and for biofilm-forming *P. aeruginosa*, the MBC value was merely twice that of the pure IL, highlighting its superior performance. This work provides a new pathway for Br_2 generation, where the strong interaction between the zeolite framework and the ionic liquid cation creates a unique catalytic microenvironment capable of activating molecular oxygen to oxidize bromide ions, providing a new way for the design of safe, efficient, and stable halogen-based antibacterial materials. Future studies will systematically investigate the influence of the HZSM-5 Si/Al ratio on the confinement stability, Br_2 generation efficiency and release kinetics. Ultimately, establishing a comprehensive structure–activity relationship will facilitate the rational design of advanced zeolite-confined IL systems. The development of this HZSM-5–*n*IL composite not only provides a promising platform for combating antimicrobial resistance but also broadens the horizon for the practical application of ionic liquids in diverse fields.

4 Experimental section

4.1 Materials

1-Methylimidazole (1-MI, 99%) and 1-bromotetradecane ($C_{14}H_{29}Br$, 98%) were purchased from Aladdin Biological Technology Co. Ltd. (Shanghai, China). Ethanol (C_2H_5OH, AR) and ethyl acetate ($C_4H_8O_2$, AR) were purchased from Beijing Chemical Co. (Beijing, China). HZSM-5 ($nSiO_2/nAl_2O_3$ = 25) was a commercial product and was purchased from Nankai University Catalyst Co. Ltd. (Tianjin, China).

Escherichia coli (*E. coli*) ATCC 25922, *Staphylococcus aureus* (*S. aureus*) ATCC 6538, *Pseudomonas aeruginosa* (*P. aeruginosa*) ATCC 9027 and drug-resistant strain *Staphylococcus aureus*

(*MRSA*) ATCC 44300 were purchased from Beijing Zhongke Zhijian Biotechnology Co., Ltd. All bacterial strains used in this study were stored at 2–8 °C according to the manufacturer's directions. *E. coli* and *S. aureus* were sub-cultured to Müller–Hinton-agar (MHA; BD Company, USA) while *P. aeruginosa* and *MRSA* were sub-cultured to trypticase soy agar (TSA; BD Company, USA) before testing.

4.2 Preparation of IL and HZSM-5/ionic liquid composites

The IL (C_{14}minBr) was synthesized *via* a modified method described in the literature.[59,60] 1-Methylimidazole (82.1 g, 1.00 mol) and 1-bromotetradecane (1.05 mol, 277.28 g) were mixed and heated at 100 °C under a N_2 atmosphere. Then the prepared solid products were purified *via* recrystallisation from boiling ethyl acetate three times and then dried in a vacuum oven at 65 °C for 24 h. The as-prepared ionic liquid was introduced into HZSM-5 (nSiO$_2$/nAl$_2$O$_3$ = 25) zeolite by an isovolumetric impregnation method using anhydrous ethanol as the solvent. The mass ratios of HZSM-5 to IL were 1 : 2, 1 : 1, 1 : 0.5, 1 : 0.35, and 1 : 0.25 and the samples were named HZSM-5–2IL, HZSM-5–1IL, HZSM-5–0.5IL, HZSM-5–0.35IL, and HZSM-5–0.25IL, respectively.

4.3 Antibacterial assay

A disk diffusion method and a broth microdilution method were used to evaluate the antibacterial activity of all samples. MHA and TSA were prepared, sterilized by autoclaving at 121 °C for 20 min, then cooled at 45–50 °C and poured into sterile Petri plates. A single colony of each bacteria strain was carefully isolated using a sterile inoculating loop and then grown in Luria-Bertani broth (*S. aureus* and *E. coli*) and tryptic soy broth (*MRSA* and *P. aeruginosa*) respectively at 37 °C overnight to prepare the bacterial suspension. Each bacterial suspension was adjusted to a turbidity of an optical density at 600 nm, equivalent to ~1 × 10^8 CFU mL^{-1}. 100 μl of the bacterial suspension containing approximately 1 × 10^7 CFU was uniformly spread on the as-prepared solidified MHA and TSA plates. The thin pellet with a diameter of 12 mm prepared using 0.1 g of each IL-containing sample and filter paper discs with a diameter of 12 mm containing 0.05 g IL was placed on the aforementioned agar plates. The plates were incubated for 24 h at 37 °C for test bacteria and all tests were performed in triplicate.

Broth microdilution method: serial two-fold dilutions of each sample in broth were prepared in 96-well microtiter plates over the range 0.00005–1% w/v. The inoculum to be tested was prepared by adjusting the turbidity of an actively overnight growing culture in broth to an optical density at 600 nm equivalent to 1 × 10^8 CFU mL^{-1}. The suspension was further diluted to provide a final inoculum density of 1 × 10^6 CFU mL^{-1} in broth as verified by the total viable count. The bacterial suspension to be tested (100 μL, 1 × 10^8 CFU mL^{-1}) was added to each well of the microdilution trays, which were incubated aerobically for 24 h at 37 °C. Positive and negative growth controls were included in each assay (6 replicates). After determination of the minimum inhibitory concentration (MIC), the minimum bactericidal concentration (MBC) was determined by spreading 20 μL of suspension from wells showing no growth onto MHA plates, which were then incubated for 24 h and examined for 99.9% killing.

4.4 Live/dead fluorescence staining

The green fluorescent dye SYTO™ 9 (λ_{ex} = 485 nm, λ_{em} = 498 nm) and red-fluorescent dye propidium iodide (PI) (λ_{ex} = 535 nm, λ_{em} = 617 nm) were used to mark live bacterial cells and dead bacteria. After treatment with IL and HZSM-5–nIL composites, bacteria were harvested by centrifugation (3500 rpm, 5 min) and stained with SYTO™ 9 and PI for 30 min at ambient temperature. Then, the bacterial suspension (5 mL) was dropped on a glass slide for microscopic observation.[61]

4.5 Measurement of intracellular ROS

After mixing IL and HZSM-5–nIL composites (50 μg mL^{-1}) for 30 min, the bacteria were immediately accumulated by centrifugation (3000 rpm, 5 min) and incubated with DCFH-DA for 30 min at 37 °C. And the bacterial suspension was washed with sterilized water and was dropped on a glass slide for microscopic observation (λ_{ex} = 488 nm, λ_{em} = 530 nm).[61]

Descriptions of the experiments in enough detail should be provided so that a skilled researcher is able to repeat them. Standard techniques and methods used throughout the work should just be stated at the beginning of the section; descriptions of these are not needed. Any unusual hazards about the chemicals, procedures or equipment should be clearly identified. Authors are encouraged to make use of the SI for lengthy synthetic sections.

Conflicts of interest

The authors declare no conflict of interest.

Data availability

Data for this work are provided in the supplementary information (SI) and any additional or raw data are available upon reasonable request from the authors.

Supplementary information: the SI includes: photographs showing the visual appearance of the HZSM-5 and the HZSM-5–nIL composites; a table summarizing the BET surface area and pore volume data; SEM images and SEM-EDS elemental mapping of the composites; XRD patterns of the composites; high-resolution XPS spectra of Si 2p, Al 2p, O 1s and N 1s; a table of the zone of inhibition diameters values; and a table of minimum inhibitory concentration (MIC) and minimum bactericidal concentration (MBC) values. See DOI: https://doi.org/10.1039/d6im00093b.

Acknowledgements

This work was financially supported by the National Natural Science Foundation of China (No. 22421003).

References

1 M. Naghavi, S. E. Vollset, K. S. Ikuta, L. R. Swetschinski, A. P. Gray, E. E. Wool, G. R. Aguilar, T. Mestrovic, G. Smith and C. Han, Global burden of bacterial antimicrobial resistance 1990–2021: A systematic analysis with forecasts to 2050, *Lancet*, 2024, **404**, 1199–1226.

2 R. Scaffaro, F. Lopresti, D. Arrigo, M. Marino and A. Nostro, Efficacy of poly (lactic acid)/carvacrol electrospun membranes against Staphylococcus aureus and Candida albicans in single and mixed cultures, *Appl. Microbiol. Biotechnol.*, 2018, **102**, 4171–4181.

3 T. Fadiji, M. Rashvand, M. O. Daramola and S. A. Iwarere, A review on antimicrobial packaging for extending the shelf life of food, *Processes*, 2023, **11**, 590.

4 W. Xie, Z.-M. Gao, W.-P. Pan, D. Hunter, A. Singh and R. Vaia, Thermal Degradation Chemistry of Alkyl Quaternary Ammonium Montmorillonite, *Chem. Mater.*, 2001, **13**, 2979–2990.

5 Z. Chegini, A. Shariati, M. Y. Alikhani, M. Safaiee, S. Rajaeih, M. Arabestani and M. Azizi, Antibacterial and antibiofilm activity of silver nanoparticles stabilized with C-phycocyanin against drug-resistant Pseudomonas aeruginosa and Staphylococcus aureus, *Front. Bioeng. Biotechnol.*, 2024, **12**, 1455385.

6 T. Welton, Room-temperature ionic liquids. Solvents for synthesis and catalysis, *Chem. Rev.*, 1999, **99**, 2071–2084.

7 S. Zhang, J. Zhang, Y. Zhang and Y. Deng, Nanoconfined ionic liquids, *Chem. Rev.*, 2017, **117**, 6755–6833.

8 T. Zhou, C. Gui, L. Sun, Y. Hu, H. Lyu, Z. Wang, Z. Song and G. Yu, Energy applications of ionic liquids: Recent developments and future prospects, *Chem. Rev.*, 2023, **123**, 12170–12253.

9 Z. Fang, X. Zheng, L. Li, J. Qi, W. Wu and Y. Lu, Ionic liquids: Emerging antimicrobial agents, *Pharm. Res.*, 2022, **39**, 2391–2404.

10 M. M. Fernandes, E. O. Carvalho, D. M. Correia, J. M. Esperança, J. Padrão, K. Ivanova, J. Hoyo, T. Tzanov and S. Lanceros-Mendez, Ionic liquids as biocompatible antibacterial agents: A case study on structure-related bioactivity on Escherichia coli, *ACS Appl. Bio Mater.*, 2022, **5**, 5181–5189.

11 Y. Hu, Y. Xing, P. Ye, H. Yu, X. Meng, Y. Song, G. Wang and Y. Diao, The antibacterial activity and mechanism of imidazole chloride ionic liquids on Staphylococcus aureus, *Front. Microbiol.*, 2023, **14**, 1109972.

12 A. D. Tikhomirov, K. S. Egorova and V. P. Ananikov, Designing effective antimicrobial agents: Structural insights into the antibiofilm activity of ionic liquids, *J. Med. Chem.*, 2025, **68**, 2105–2123.

13 M. Galluzzi, L. Marfori, S. Asperti, A. De Vita, M. Giannangeli, A. Caselli, P. Milani and A. Podestà, Interaction of imidazolium-based ionic liquids with supported phospholipid bilayers as model biomembranes, *Phys. Chem. Chem. Phys.*, 2022, **24**, 27328–27342.

14 N. Nikfarjam, M. Ghomi, T. Agarwal, M. Hassanpour, E. Sharifi, D. Khorsandi, M. Ali Khan, F. Rossi, A. Rossetti and E. Nazarzadeh Zare, Antimicrobial ionic liquid-based materials for biomedical applications, *Adv. Funct. Mater.*, 2021, **31**, 2104148.

15 W. P. Smith, B. R. Wucher, C. D. Nadell and K. R. Foster, Bacterial defences: Mechanisms, evolution and antimicrobial resistance, *Nat. Rev. Microbiol.*, 2023, **21**, 519–534.

16 S. B. Levy, Antimicrobial resistance: Bacteria on the defence, *BMJ*, 1998, **317**, 612–613.

17 A. Jousset, Ecological and evolutive implications of bacterial defences against predators, *Environ. Microbiol.*, 2012, **14**, 1830–1843.

18 L.-Y. Zhang, S.-H. Liu and Y. Wang, Exploring the influence of the type of anion in imidazolium ionic liquids on its thermal stability, *J. Therm. Anal. Calorim.*, 2023, **148**, 4985–4995.

19 L. Wang, L. Li, Q. Fan, T. Chu, Y. Wang and Y. Xu, Thermal stability and flammability of several quaternary ammonium ionic liquids, *J. Mol. Liq.*, 2023, **382**, 121920.

20 Y. Chen, X. Han, Z. Liu, Y. Li, H. Sun, H. Wang and J. Wang, Thermal decomposition and volatility of ionic liquids: Factors, evaluation and strategies, *J. Mol. Liq.*, 2022, **366**, 120336.

21 S. F. Kurtoğlu-Öztulum, A. Jalal and A. Uzun, Thermal stability limits of imidazolium, piperidinium, pyridinium, and pyrrolidinium ionic liquids immobilized on metal oxides, *J. Mol. Liq.*, 2022, **363**, 119804.

22 P. Kumari, V. V. Pillai and A. Benedetto, Mechanisms of action of ionic liquids on living cells: The state of the art, *Biophys. Rev.*, 2020, **12**, 1187–1215.

23 D. O. Hartmann, K. Shimizu, F. Siopa, M. C. Leitão, C. A. Afonso, J. N. C. Lopes and C. S. Pereira, Plasma membrane permeabilisation by ionic liquids: A matter of charge, *Green Chem.*, 2015, **17**, 4587–4598.

24 C. M. Mendonça, D. T. Balogh, S. C. Barbosa, T. E. Sintra, S. P. Ventura, L. F. Martins, P. Morgado, E. J. Filipe, J. A. Coutinho and O. N. Oliveira, Understanding the interactions of imidazolium-based ionic liquids with cell membrane models, *Phys. Chem. Chem. Phys.*, 2018, **20**, 29764–29777.

25 X. Song, R. Tian and K. Liu, Recent advances in the application of ionic liquids in antimicrobial material for air disinfection and sterilization, *Front. Cell. Infect. Microbiol.*, 2023, **13**, 1186117.

26 V. Sharma, J. Gupta, J. B. Mitra, H. Srinivasan, V. G. Sakai, S. Ghosh and S. Mitra, The physics of antimicrobial activity of ionic liquids, *J. Phys. Chem. Lett.*, 2024, **15**, 7075–7083.

27 E. Novello, G. Scalzo, G. D'Agata, M. G. Raucci, L. Ambrosio, A. Soriente, B. Tomasello, C. Restuccia, L. Parafati and G. M. Consoli, Synthesis, characterisation, and in vitro evaluation of biocompatibility, antibacterial and antitumor activity of imidazolium ionic liquids, *Pharmaceutics*, 2024, **16**, 642.

28 A. Abbaszadegan, A. Gholami, S. Abbaszadegan, Z. S. Aleyasin, Y. Ghahramani, S. Dorostkar, B. Hemmateenejad, Y. Ghasemi and H. Sharghi, The effects of different ionic liquid coatings and the length of alkyl chain on antimicrobial and cytotoxic properties of silver nanoparticles, *Iran. Endod. J.*, 2017, **12**, 481.

29 E. Avirdi, H. K. Paumo, B. P. Kamdem, M. B. Singh, K. Kumari, L. Katata-Seru and I. Bahadur, Imidazolium-based ionic liquid-assisted silver nanoparticles and their antibacterial activity: Experimental and density functional theory studies, *ACS Omega*, 2023, **8**, 42976–42986.

30 X. Yang, K. Quan, J. Wang, J. Liu, B. Liu, J. Chen, M. Guan and H. Qiu, Particle size and pore adjustment of dendritic mesoporous silica using different long alkyl-chain imidazolium ionic liquids as templates, *Microporous Mesoporous Mater.*, 2022, **345**, 112249.
31 D. Bains, G. Singh, N. Kaur and N. Singh, Development of an ionic liquid@metal-based nanocomposite-loaded hierarchical hydrophobic surface to the aluminum substrate for antibacterial properties, *ACS Appl. Bio Mater.*, 2020, **3**, 4962–4973.
32 S. Kumar, A. Sindhu and P. Venkatesu, Ionic liquid-modified gold nanoparticles for enhancing antimicrobial activity and thermal stability of enzymes, *ACS Appl. Nano Mater.*, 2021, **4**, 3185–3196.
33 X. Li, W. Du, W. Xu, G. Ling and P. Zhang, Dissolving microneedles based on ZnO nanoparticles and an ionic liquid as synergistic antibacterial agents, *J. Mater. Chem. B*, 2023, **11**, 4354–4364.
34 L. G. da Trindade, L. Zanchet, A. B. Trench, J. C. Souza, M. H. Carvalho, A. J. de Oliveira, E. C. Pereira, T. M. Mazzo and E. Longo, Flower-like ZnO/ionic liquid composites: Structure, morphology, and photocatalytic activity, *Ionics*, 2019, **25**, 3197–3210.
35 D. Bains, G. Singh, J. Bhinder, P. K. Agnihotri and N. Singh, Ionic liquid-functionalized multiwalled carbon nanotube-based hydrophobic coatings for robust antibacterial applications, *ACS Appl. Bio Mater.*, 2020, **3**, 2092–2103.
36 C. Liu, S. Qiu, P. Du, H. Zhao and L. Wang, An ionic liquid–graphene oxide hybrid nanomaterial: synthesis and anticorrosive applications, *Nanoscale*, 2018, **10**, 8115–8124.
37 J. Leng, X. Liu, Y. Xu, S.-E. Zhu, Y. Zhang, Z. Tan, X. Yang, J.-E. Jin, Y. Shi and H. Fan, Evaluation of the alkyl chain length and photocatalytic antibacterial performance of cation g-C_3N_4, *J. Mater. Chem. B*, 2025, **13**, 264–273.
38 A. Lv, X. Lv, X. Xu, Y. Chen, J. Zhang and Z.-B. Shao, Tailored multifunctional composite hydrogel based on chitosan and quaternary ammonium ionic liquids@montmorillonite with different chain lengths for effective removal of dyes and 4-nitrophenol, *Sep. Purif. Technol.*, 2024, **342**, 127019.
39 H. Bujdáková, V. Bujdáková, H. Májeková-Koščová, B. Gaálová, V. Bizovská, P. Boháč and J. Bujdák, Antimicrobial activity of organoclays based on quaternary alkylammonium and alkylphosphonium surfactants and montmorillonite, *Appl. Clay Sci.*, 2018, **158**, 21–28.
40 D. Li, X. Huang, F. Hao, Y. Lv, H. Chen, S. Wu, W. Xiong, P. Liu and H. A. Luo, Preparation of organic-inorganic composites with high antibacterial activity based on sepiolite, chitosan and zinc: The study of the active antibacterial sites of chitosan-zinc oxide structure, *Appl. Clay Sci.*, 2022, **216**, 106325.
41 A. Szymura, S. Ilyas, F. Grohmann and S. Mathur, Ionic liquid modified mesoporous silica nanocarriers for efficient drug delivery and hydrophobic surface engineering, *Mater. Adv.*, 2025, **6**, 4220–4232.
42 A. Bernardos, E. Piacenza, F. Sancenon, M. Hamidi, A. Maleki, R. J. Turner and R. Martínez-Máñez, Mesoporous silica-based materials with bactericidal properties, *Small*, 2019, **15**, 1900669.
43 D. Hodyna, J.-F. Bardeau, L. Metelytsia, S. Riabov, L. Kobrina, S. Laptiy, L. Kalashnikova, V. Parkhomenko, O. Tarasyuk and S. Rogalsky, Efficient antimicrobial activity and reduced toxicity of 1-dodecyl-3-methylimidazolium tetrafluoroborate ionic liquid/β-cyclodextrin complex, *Chem. Eng. J.*, 2016, **284**, 1136–1145.
44 B. Sarkar, K. Das, T. Saha, E. Prasad and R. L. Gardas, Insights into the formations of host–guest complexes based on the Benzimidazolium based ionic liquids–β-cyclodextrin systems, *ACS Phys. Chem. Au*, 2021, **2**, 3–15.
45 V. Paunovic, S. Mitchell, R. Verel, S. S. Lee and J. Pérez-Ramírez, Aluminum redistribution in ZSM-5 zeolite upon interaction with gaseous halogens and hydrogen halides and implications in catalysis, *J. Phys. Chem. C*, 2019, **124**, 722–733.
46 I. Bucsi and G. A. Olah, Selective monochlorination of methane over solid acid and zeolite catalysts, *Catal. Lett.*, 1992, **16**, 27–38.
47 H. Joo, D. Kim, K. S. Lim, Y. N. Choi and K. Na, Selective methane chlorination to methyl chloride by zeolite Y-based catalysts, *Solid State Sci.*, 2018, **77**, 74–80.
48 V. Paunović and J. Pérez-Ramírez, Catalytic halogenation of methane: A dream reaction with practical scope?, *Catal. Sci. Technol.*, 2019, **9**, 4515–4530.
49 Y. Liu, H. Tao, X. Yang, X. Wu, J. Li, C. Zhang, R. T. Yang and Z. Li, Adsorptive purification of NO_x by HZSM-5 zeolites: Effects of Si/Al ratio, temperature, humidity, and gas composition, *Microporous Mesoporous Mater.*, 2023, **348**, 112331.
50 K. Chen, Z. Gan, S. Horstmeier and J. L. White, Distribution of aluminum species in zeolite catalysts: 27Al NMR of framework, partially-coordinated framework, and non-framework moieties, *J. Am. Chem. Soc.*, 2021, **143**, 6669–6680.
51 Y. He, M. A. Khan, A. D. Drake, J. Garay, A. Shirodkar, S. Goodlett, J. Strzalka, F. Ladipo, B. L. Knutson and S. E. Rankin, Crystallization of nanopore-confined imidazolium ionic liquids probed by temperature-resolved in situ grazing-incidence wide angle X-ray scattering (GIWAXS), *Nanoscale Adv.*, 2025, **7**, 6607–6619.
52 World Health Organization, Alternative drinking-water disinfectants: Bromine, iodine and silver, 2018, https://www.who.int/publications/i/item/9789241513692, (accessed March 2026).
53 L. M. Mashburn and M. Whiteley, Membrane vesicles traffic signals and facilitate group activities in a prokaryote, *Nature*, 2005, **437**, 422–425.
54 L. Turnbull, M. Toyofuku, A. L. Hynen, M. Kurosawa, G. Pessi, N. K. Petty, S. R. Osvath, G. Cárcamo-Oyarce, E. S. Gloag and R. Shimoni, Explosive cell lysis as a mechanism for the biogenesis of bacterial membrane vesicles and biofilms, *Nat. Commun.*, 2016, **7**, 11220.
55 C. Schwechheimer and M. J. Kuehn, Outer-membrane vesicles from Gram-negative bacteria: Biogenesis and functions, *Nat. Rev. Microbiol.*, 2015, **13**, 605–619.
56 J. Gutknecht, L. Bruner and D. Tosteson, The permeability of thin lipid membranes to bromide and bromine, *J. Gen. Physiol.*, 1972, **59**, 486–502.
57 R. M. Heredia, P. S. Boeris, A. S. Liffourrena, M. F. Bergero, G. A. Lopez and G. I. Lucchesi, Release of outer membrane vesicles in Pseudomonas putida as a response to stress

caused by cationic surfactants, *Microbiology*, 2016, **162**, 813–822.

58 L. A. Rowe, N. Degtyareva and P. W. Doetsch, DNA damage-induced reactive oxygen species (ROS) stress response in Saccharomyces cerevisiae, *Free Radical Biol. Med.*, 2008, **45**, 1167–1177.

59 L. Carson, P. K. Chau, M. J. Earle, M. A. Gilea, B. F. Gilmore, S. P. Gorman, M. T. McCann and K. R. Seddon, Antibiofilm activities of 1-alkyl-3-methylimidazolium chloride ionic liquids, *Green Chem.*, 2009, **11**, 492–497.

60 J. Łuczak, C. Jungnickel, I. Łącka, S. Stolte and J. Hupka, Antimicrobial and surface activity of 1-alkyl-3-methylimidazolium derivatives, *Green Chem.*, 2010, **12**, 593–601.

61 J. Xiong, Y. Cao, H. Zhao, J. Chen, X. Cai, X. Li, Y. Liu, H. Xiao and J. Ge, Cooperative antibacterial enzyme-Ag-polymer nanocomposites, *ACS Nano*, 2022, **16**, 19013–19024.